Bio-Design and Manufacturing (2023) 6:174–188
https://doi.org/10.1007/s42242-023-00239-1

RESEARCH ARTICLE

# Numerical simulation and printability analysis of fused deposition modeling with dual-temperature control

Xiaodan Huo[1,2] · Bin Zhang[1] · Qianglong Han[1,2] · Yong Huang[3] · Jun Yin[1,2]

Received: 24 December 2022 / Accepted: 2 February 2023 / Published online: 3 March 2023


## Abstract

Ideal tissue engineering scaffolds need interconnected pores and high porosity to enable cell survival, migration, proliferation, and differentiation. However, obtaining a high-resolution structure is difficult with traditional one-temperature control fused deposition modeling (FDM). In this study, we propose a dual-temperature control method to improve printability. A numerical model is developed in which the viscosity is a function of temperature and shear rate to study the influence of two different temperature control modes. Quantitative tests are used to assess filament formation and shape fidelity, including one-dimensional filament printing, deposition at corners, fusion, and collapse. By using dual-temperature control, the width of the deposited poly(ε-caprolactone) filament is reduced to 50 μm. The comparative results of both the experimental method and numerical simulation suggest that the dual-temperature control FDM can manufacture spatially arranged constructs and presents a promising application in tissue engineering.

Xiaodan Huo and Bin Zhang have contributed equally to this work.

✉ Yong Huang
yongh@ufl.edu

✉ Jun Yin
junyin@zju.edu.cn

[1] The State Key Laboratory of Fluid Power and Mechatronic Systems, School of Mechanical Engineering, Zhejiang University, Hangzhou 310028, China

[2] Key Laboratory of 3D Printing Process and Equipment of Zhejiang Province, School of Mechanical Engineering, Zhejiang University, Hangzhou 310028, China

[3] Department of Mechanical and Aerospace Engineering, University of Florida, Gainesville, FL 32611, USA

**Graphic abstract**

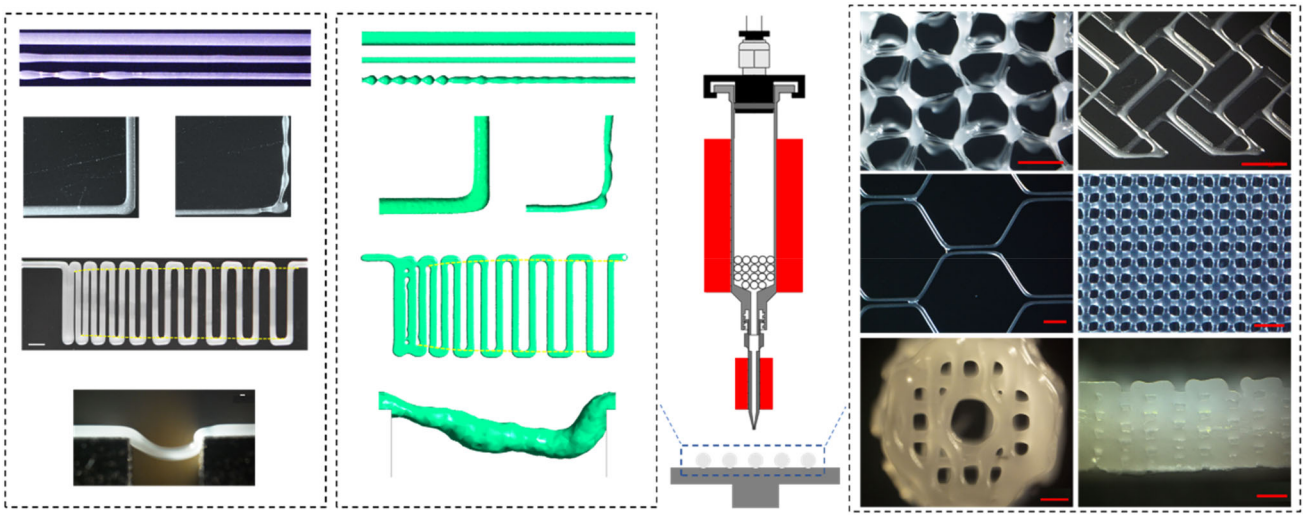

**Keywords** Fused deposition modeling (FDM) · Dual-temperature control · Filament deposition · Printing resolution · Viscosity

## Introduction

Biomedical polymers, namely poly(lactic acid) (PLA) [1], poly(ε-caprolactone) (PCL) [2], and poly(lactic-co-glycolic) acid (PLGA) [3], are popular scaffold materials for tissue engineering. Compared with ceramics and metals [4–6], polymers have better biocompatibility, a more controllable degradation rate, and excellent processability. Conventionally, polymer scaffolds are fabricated by using salt leaching [7], solvent casting [8], gas foaming [9], and phase separation [10]. However, conventional fabrication techniques generally lack the capability to construct regular porous structures, and fully removing toxic organic solvents after fabrication is difficult, resulting in the poor biocompatibility of conventional polymeric scaffolds [11]. Recently, three-dimensional (3D) printing technologies [12], including extrusion-based printing [13], selective laser sintering [14], and melt electrospinning writing [15], have developed rapidly. Compared with conventional manufacturing technologies, 3D printing technologies present several advantages in tissue engineering, including high printing resolution, fast fabrication speed, and the ability to customize objects to meet the demands of specific applications [16–20].

A widely used 3D printing method is fused deposition modeling (FDM), which is easier to implement than other 3D printing methods [21–25]. During FDM, thermoplastic polymeric materials are melted at the nozzle and extruded as filaments, which are deposited and fused layer-by-layer onto the receiving platform to solidify into final parts [26, 27]. FDM can precisely control the diameter and location of deposited filaments, resulting in overall control of scaffold shape and pore morphology [21]. In addition, FDM has no toxic chemical solvents that need removal in tissue scaffold fabrication [28–30]. Based on these aforementioned advantages, FDM has been used to print different polymers, including PLA and its copolymer [31] and PCL [32–36]. Recently, research has increasingly focused on the FDM of PCL as a tissue engineering scaffold. By using two lay-down patterns, 0°/90° and 0°/60°/120°, Zein et al. [34] manufactured PCL scaffolds with different pore shapes and a fully interconnected channel network. Zhang et al. [35] fabricated PCL scaffolds with different pore sizes for meniscus tissue engineering; the PCL scaffold with a mean pore size of 215 μm demonstrated optimized cell behaviors, extracellular matrix (ECM) production and deposition, and the resultant mechanical properties. Manjunath et al. [37] used FDM to fabricate PLA/PCL composites to improve the Young's modulus of bone tissue engineering scaffolds.

The ideal tissue engineering scaffolds must have interconnected pores and high porosity to ensure cell migration, nutrition diffusion, and metabolic waste removal [38–41]. Larger pores in scaffolds are conducive to cell diffusion and migration, whereas smaller pores provide a higher scaffold surface area for cell adhesion [34, 35]. Therefore, the accurate control of the porosity and pore size of tissue engineering scaffolds is of great importance. Previous literature rarely reports achieving FDM-printed PCL filaments with a diameter smaller than 200 μm, which is much larger than the

dimension of cells (less than 50 μm) [42, 43]. Thus, printing PCL tissue engineering scaffolds with a smaller size and high porosity using FDM is difficult. Efforts have been made to increase the printing resolution of FDM. Kumar et al. [44] reduced the width of FDM-printed filaments by 42.42% when the printing speed was increased from 700 to 1300 mm/min, but the filament diameter was still larger than 1 mm. Hıra et al. [45] used the optimized nozzle channel geometries to improve the dimensional accuracy (deviation of width is within 6%–8%) of the FDM-printed acrylonitrile butadiene styrene (ABS), PLA, and chlorinated polyethylene (CPE) parts, but the optimization mechanism of the nozzle geometry was difficult to extend to other printers.

Generally, in most FDM printers, the one-temperature control system is implemented, and the temperature control is set on the metal printing syringe (Fig. 1a). Thus, the temperature gradient clearly decreases from the syringe to the nozzle, leading to a much lower temperature at the nozzle outlet than the setting temperature. Therefore, controlling the needle temperature by regulating the syringe temperature is highly difficult. Moreover, the viscosity of the melting polymer fluid is sensitive to printing temperature, and a higher viscosity results in poor or even failed extrusion, while a lower viscosity leads to the melt spreading of the polymeric filament. Therefore, accurate control of the printing temperature is of great importance for FDM of thermoplastic polymers. Based on this contradiction, this study proposes dual-temperature control of FDM printing. A higher heating temperature is applied at the syringe to improve the fluidity of the upper part of the melt PCL, while a lower temperature is applied at the needle to achieve better formability of the extruded PCL.

In this study, we present a viable, cost-effective, and simple process modification to decrease the filament width to 50 μm and below by changing the traditional one-temperature control to dual-temperature control. Using experimental methods and numerical simulations, this study explores the printability with different temperature control modes and examines the mechanism by which dual-temperature control has better printability than one-temperature control. By using dual-temperature control, the width of the deposited PCL filament is reduced, and the printability of the FDM is improved, thereby providing a new idea for further application of PCL scaffolds in tissue engineering.

## Materials and methods

### Materials and characterization

Melted PCL (Mw=150,000) with a density of 1146 kg/m$^3$ was purchased from Daigang Biomaterial (Jinan, China). The thermal conductivity coefficient and specific heat capacity of PCL were tested using a flash thermal conductance tester (DXF500, USA) and were found to be 0.203 W/(m·K) and 1843 J/(kg·K), respectively. Images of deposited filaments were taken with an optical microscope (Nikon AZ100, Japan) for further measurements.

The rheological properties of the melted PCL were determined using a fast-rotating rheometer (MCR102, Anton Paar, Austria). The experiments were performed by using a 25-mm diameter parallel-plate configuration (diameter 25 mm, gap 1 mm). Experiments on the temperature and viscosity of PCL samples were carried out at 60 °C and 140 °C in a step of 2 °C as the shear rates ranged from 0.1 to 4 s$^{-1}$. Subsequently, experiments on the shear rate and viscosity were carried out on PCL samples with temperatures ranging from 65–140 °C and shear rates of 0.1–30 s$^{-1}$.

### FDM with dual-temperature control

To achieve an appropriate temperature at the printing nozzle outlet, we propose dual-temperature control (Fig. 1a). A higher heating temperature was applied at the syringe (high-temperature heating zone) for PCL melting, while a lower temperature was applied at the needle (low-temperature heating zone). When the melted PCL flowed from the high-temperature heating zone to the low-temperature heating zone, the printing temperature gradually decreased, and the rheology of melted PCL became appropriate for extrusion.

The FDM printing platform consists of a 3D motion platform, a system of air pressure mediation and a temperature controller. Figure 1a shows the schematic diagram of the printing head. In dual-temperature control, a long needle (17 mm) was used and wrapped with a syringe with an aluminum heating block. By comparison, the one-temperature control used a short needle (7 mm), and only the syringe was wrapped with an aluminum heating block. The temperature sensor was used to provide an accurate actual temperature for proportional-integral-derivative (PID) control to precisely control the heating temperature. Needles with different inner diameters (100 and 200 μm) were purchased from Deli Precision (Shenzhen, China). Under the control of computer software, the nozzle can move vertically ($x$–$y$ plane), and the substrate can move horizontally ($z$-direction), as shown in Fig. 1b. All printing processes were performed at room temperature.

### Numerical model of dual-temperature control FDM

In this study, the computational fluid dynamics approach was conducted to evaluate the printability of FDM printing with two temperature control modes using the software ANSYS (Ansys, Canonsburg, PA, USA). To guarantee the precision of the computational simulation, the geometry was meshed

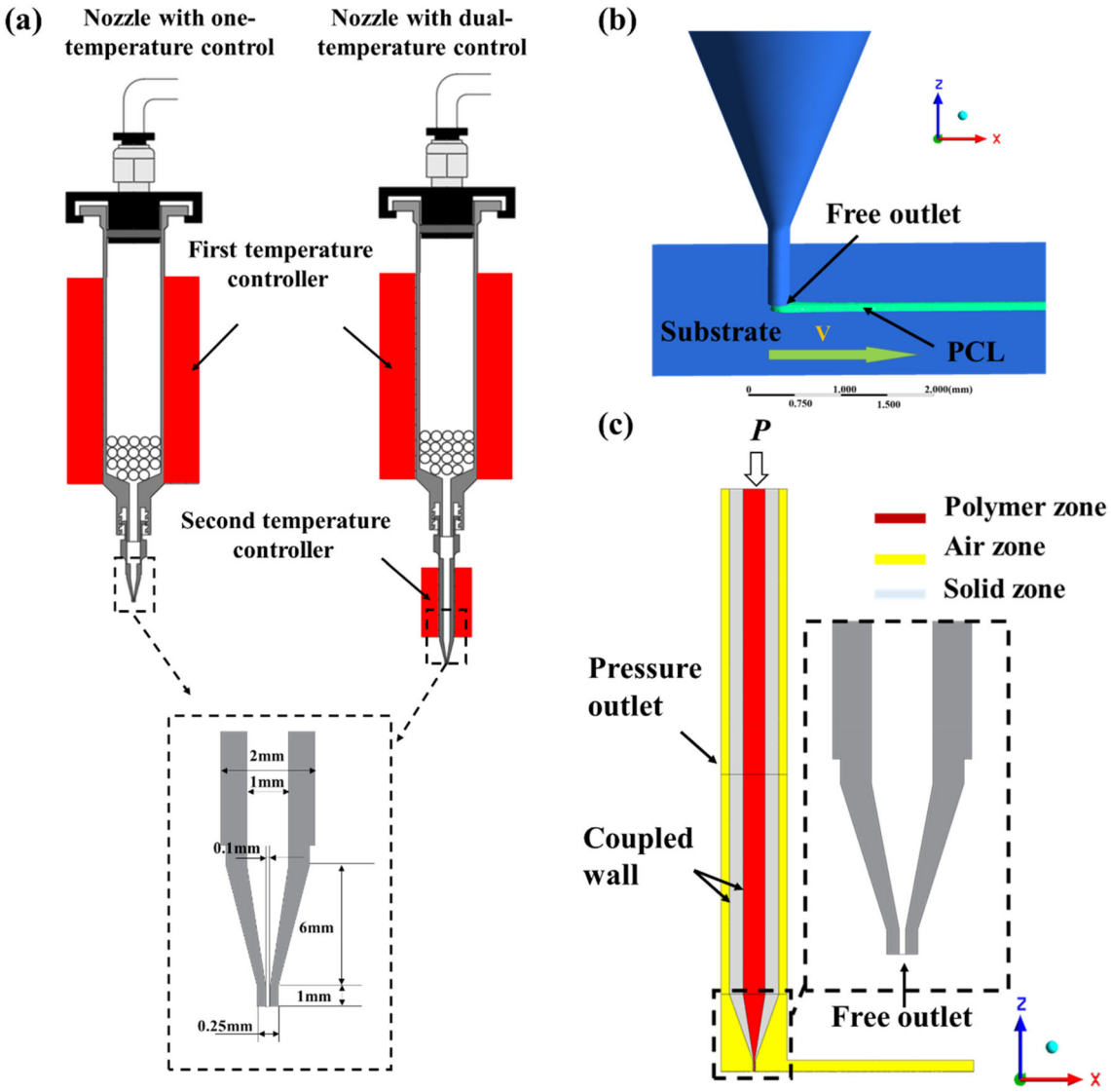


**Fig. 1** Fused deposition modeling (FDM) system: **a** schematic diagram with one- and dual-temperature control and the nozzle geometry; **b** front view of a simulation model of filament deposition; **c** geometry and boundary conditions of the numerical model (PCL: poly(ε-caprolactone))

using hexahedrons, and the maximum size of the control volumes was set as 0.02 mm. Figure 1b shows a representative image of the printed whole filament. In this numerical model, the melted PCL fluid at the nozzle is assumed to be laminar and fully developed.

### Governing equations

In the numerical simulation, the mass conservation of the incompressible flow is given as

$$\frac{\partial \rho}{\partial t} + \nabla \cdot (\rho \overrightarrow{u}) = 0 \tag{1}$$

and the Navier–Stokes equation is used to describe the melted PCL fluid flow

$$\frac{\partial}{\partial t}(\rho \overrightarrow{u}) + \rho(\overrightarrow{u} \cdot \nabla)\overrightarrow{u} = \nabla \cdot [-pI + \mu(\nabla \overrightarrow{u} + (\nabla \overrightarrow{u})^{\mathrm{T}})] + \rho \overrightarrow{g} + \overrightarrow{F_{\mathrm{st}}}, \tag{2}$$

where $\rho$ is the density, $u$ is the flow velocity, $p$ is the pressure applied to the fluid, $I$ is the identity matrix, $\mu$ is the dynamic viscosity of the fluid, $g$ is the gravity field, $F_{\mathrm{st}}$ represents the surface tension, and $t$ is time. The temperature distribution of PCL and air can be obtained by solving the energy equation:

$$\rho C_{\mathrm{p}} \vec{u} \cdot \nabla T + \nabla \cdot (-k \nabla T) = \dot{Q}, \tag{3}$$

where $C_p$ is the specific heat capacity at constant pressure, $k$ is the thermal conductivity, $\dot{Q}$ is the heat flow rate, and $T$ is temperature. The volume of fluid method is used for tracking the interface between the liquid and gas [46–50].

### Geometric model and boundary conditions

In the simulation model, plane symmetry is used on the middle plane ($x$–$z$ plane) of the nozzle in Fig. 1c. The nozzle is a cylindrical tube with inner diameter $D$ and a fixed position, while the substrate moves with a controlled (printing) speed. Below the printing head, the moving substrate is modeled by a perpendicular stiff plane, with a gap distance $H$ to the nozzle outlet. The long needle that is used in dual-temperature control has a heating section $L_1$. The syringe and the needle are filled with the melted PCL at the beginning of the simulation. With a constant inlet pressure, the melted PCL fluid is extruded and deposited onto a moving substrate. The deposited PCL gradually cooled and began to solidify when the polymer temperature was below the melting point of PCL. Notably, fixed temperature boundary conditions are used at the inlet. The temperatures of the syringe and needle of the dual-temperature control FDM were 140 and 120 °C, respectively, while those of the one-temperature control FDM were set to 120 °C. There is convective heat transfer between the wall and the air and thermal conduction between the wall and the fluid; thus, the nozzle wall is set to be coupled under thermal boundary conditions (coupled wall). Table 1 lists the necessary material properties for computational simulations.

### Constitutive equations of PCL

According to the Cross-Williams–Landel–Ferry (Cross-WLF) viscosity model [51, 52], an empirical model is proposed to describe the rheological behavior of melted PCL under different temperatures. The Cross-WLF model can be described as

$$\eta(T,\gamma)=\frac{\eta_0(T,\gamma)}{1+\left(\frac{\eta_0\dot{\gamma}}{\tau^*}\right)^{1-n}} \tag{4}$$

and

$$\eta_0(T,\gamma)=D_1\exp\left[-\frac{A_1(T-T_g)}{A_2+(T-T_g)}\right], \tag{5}$$

where viscosity ($\eta$) is a function of temperature ($T$) and shear rate ($\dot{\gamma}$), $\tau^*$ is the critical shear stress for the fluid to change into a pseudoplastic fluid, $n$ is a non-Newtonian index, $\eta_0$ is the zero-shear viscosity and is defined by Eq. (5), and $T_g$ is the glass transition temperature. When $T$ is higher than the glass transition temperature ($T_g$), the zero-shear viscosity is considered a function of temperature (Eq. (5)). $T_g$ is the reference temperature, mainly related to the glass transition temperature of the melted PCL. $D_1$, $A_1$, and $A_2$ are the material constants of melted PCL to be fitted.

**Table 1** Parameters for computational simulations

| Parameter | Definition | Value | Unit |
|---|---|---|---|
| $C_{p,a}$ | Specific heat capacity of the air | 1000 | J/(kg·K) |
| $C_{p,n}$ | Specific heat capacity of the nozzle | 500 | J/(kg·K) |
| $C_{p,p}$ | Specific heat capacity of the PCL | 1843 | J/(kg·K) |
| $C_{p,s}$ | Specific heat capacity of the substrate | 800 | J/(kg·K) |
| $D$ | Inner diameter of the nozzle | 100/200 | μm |
| $H$ | Gap distance between nozzle and substrate | 80 | μm |
| $k_a$ | Thermal conductivity coefficient of the air | 0.034 | W/(m·K) |
| $k_n$ | Thermal conductivity coefficient of the nozzle | 17 | W/(m·K) |
| $k_p$ | Thermal conductivity coefficient of the PCL | 0.203 | W/(m·K) |
| $k_s$ | Thermal conductivity coefficient of the substrate | 2.5 | W/(m·K) |
| $L_1$ | Heating length | 10 | mm |
| $L_2$ | Taper length | 6 | mm |
| $L_3$ | Capillary length | 1 | mm |
| $P$ | Air pressure | 0.4 | MPa |
| $T$ | Syringe/needle temperature | 140/120 | °C |
| $T_s$ | Atmosphere temperature | 25 | °C |
| $v$ | Printing speed | 0.2–2.1 | mm/s |
| $\eta_a$ | Viscosity of the air | $2.2\times10^{-5}$ | Pa·s |
| $\eta_p$ | Viscosity of the PCL | $\eta\,(T,\gamma)^*$ | Pa·s |
| $\rho_a$ | Density of the air | 0.9 | kg/m$^3$ |
| $\rho_n$ | Density of the nozzle | 7800 | kg/m$^3$ |
| $\rho_p$ | Density of the PCL | 1160 | kg/m$^3$ |
| $\rho_s$ | Density of the substrate | 2200 | kg/m$^3$ |
| $\sigma$ | Surface tension coefficient of the PCL in air | 1.00 | mN/m |

* This parameter is described in Section "Constitutive equations of PCL". PCL: poly(ε-caprolactone)

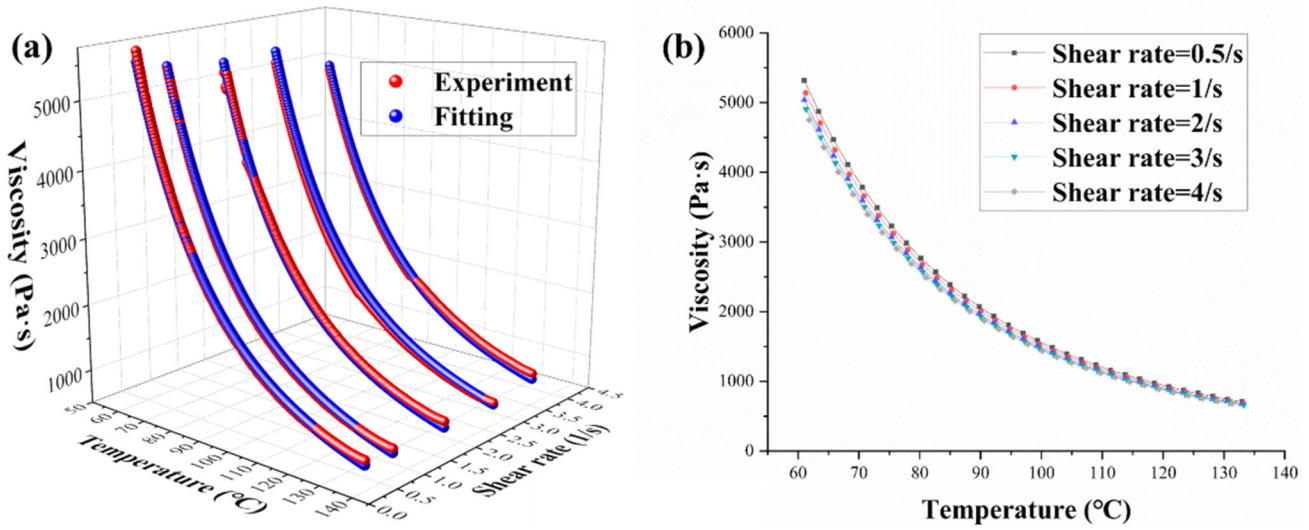


**Fig. 2** Constitutive model of melted poly(ε-caprolactone) (PCL): **a** experimental and fitted data; **b** viscosity–temperature curves of PCL at different shear rates

**Table 2** Parameters of the cross-Williams–Landel–Ferry (cross-WLF) model

| Parameter | $n$ | $\tau^*$ (Pa) | $D_1$ (Pa·s) | $T_g$ (K) | $A_1$ | $A_2$ (K) |
|---|---|---|---|---|---|---|
| Value | 0.9495 | $9.97\times10^3$ | $7.429\times10^9$ | 213.15 | 21.51 | 63.49 |

## Results and discussion

### Determining melted PCL constitutive equations

Figure 2a shows the experimental results of rheological characterization of melted PCL, and the fitting data based on the constitutive model (Eqs. (4) and (5)) are found to be in good agreement with the experimental data (Fig. 2a). Table 2 lists the fitting parameters of the PCL constitutive model.

The glass transition temperature ($T_g$) of melted PCL is approximately −60 °C. Based on the constitutive model (Eq. (4)), the melted PCL fluid demonstrates shear-thinning behavior under different temperatures. The viscosity–temperature curve under a series of shear rates is shown in Fig. 2b.

### Printing of one-dimensional (1D) filament

To compare the printability of 1D filaments with two different temperature control modes, we deposited linear fibers with different printing speeds to explore the mechanisms of formability, fiber width, and cross-sectional variation [53]. Figure 3a shows that when the printing speed was small, the melted PCL was deposited on the substrate to form continuous filaments. However, as the printing speed increased to a critical value, the filament became unstable, and continuous filaments could not be formed. Notably, the critical printing speed of the dual-temperature control FDM (2 mm/s) is greater than that of the one-temperature control FDM (1.7 mm/s). In addition, at the same printing speed, the width of the filament printed by the dual-temperature control FDM is smaller than that printed by the one-temperature control FDM, as shown in Fig. 3b. Figure 3c shows that with increasing printing speed, the cross section of the deposited filaments gradually changes from a rectangular to a circular shape. At the same printing speed, the deposited filaments printed by the dual-temperature control FDM had a higher shape fidelity, and the cross section of deposited filaments printed by one-temperature control FDM was easier to collapse.

Figures 4a1 and a2 show the radial temperature distribution at the nozzle outlet. Compared with the dual-temperature control FDM, the one-temperature control FDM has a less uniform radial temperature distribution, which leads to a less uniform viscosity distribution of the melted PCL at the nozzle outlet (Fig. 4a3). Therefore, the radial velocity distribution at the outlet is not uniform (Fig. 4a4), and the shear rate at the outlet of the one-temperature control FDM is approximately 10 times that of the dual-temperature control FDM (Fig. 4a5). Figure 4b2 shows that the viscosity of the melted PCL fluid at different positions is significantly different and smaller than that of the dual-temperature control FDM. Given the lower viscosity at the outlet of one-temperature control FDM, the outlet flow rate is larger at the same printing speed, which causes the accumulation of the melted PCL at the outlet (Fig. 3c). Therefore, the one-temperature control FDM has wider filaments during printing, meaning a lower printing resolution. The viscosity distribution at the nozzle outlet is

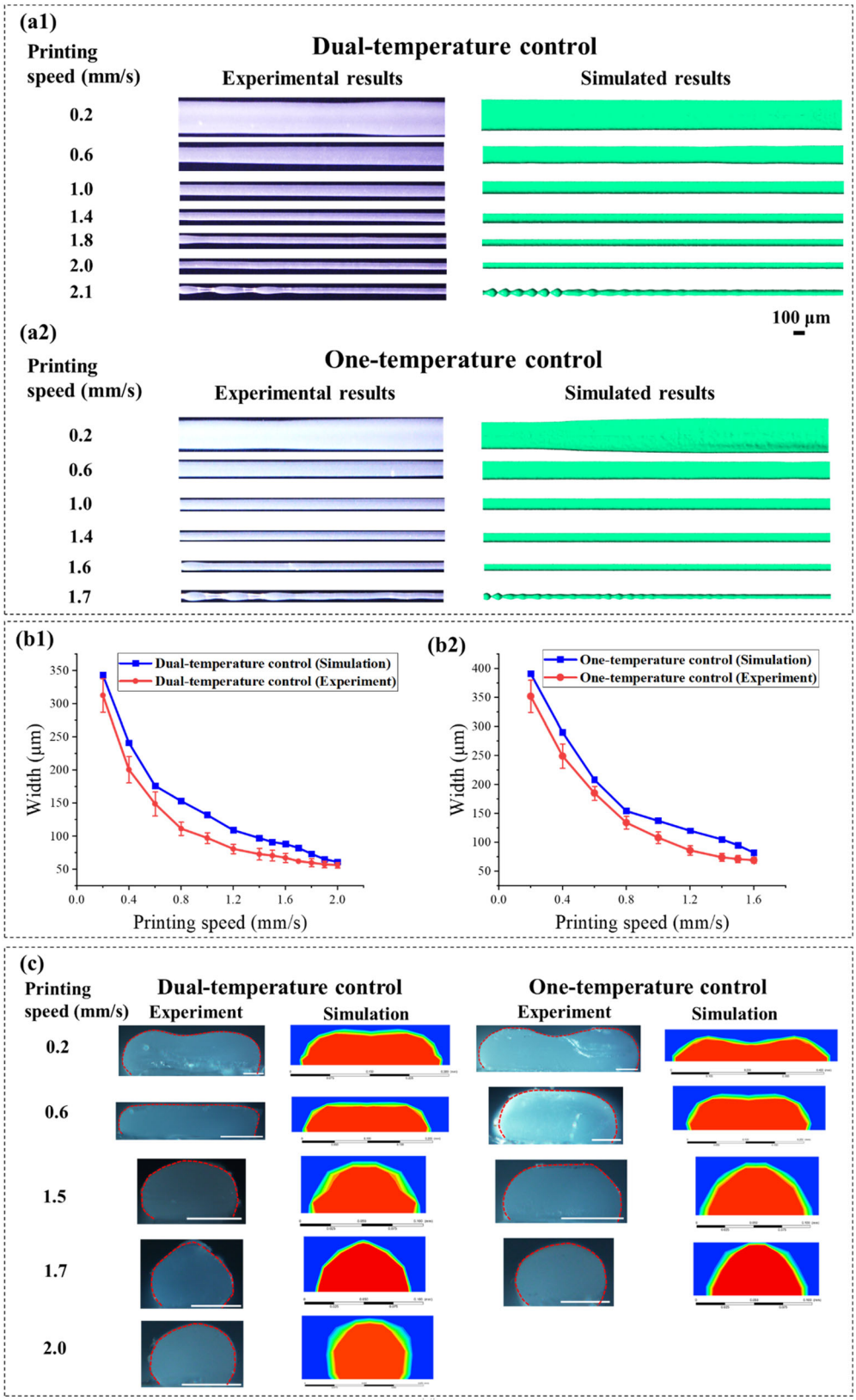


**Fig. 3** Filament printing (nozzle with an inner diameter of 100 μm): **a** experimental results and simulated results with dual- and one-temperature control; **b** filament width as a function of printing speed with dual- and one-temperature control (the blue line represents the simulated result and the red line represents the experimental result); **c** exploration of the shape of the cross section of the filament, scale bar=100 μm

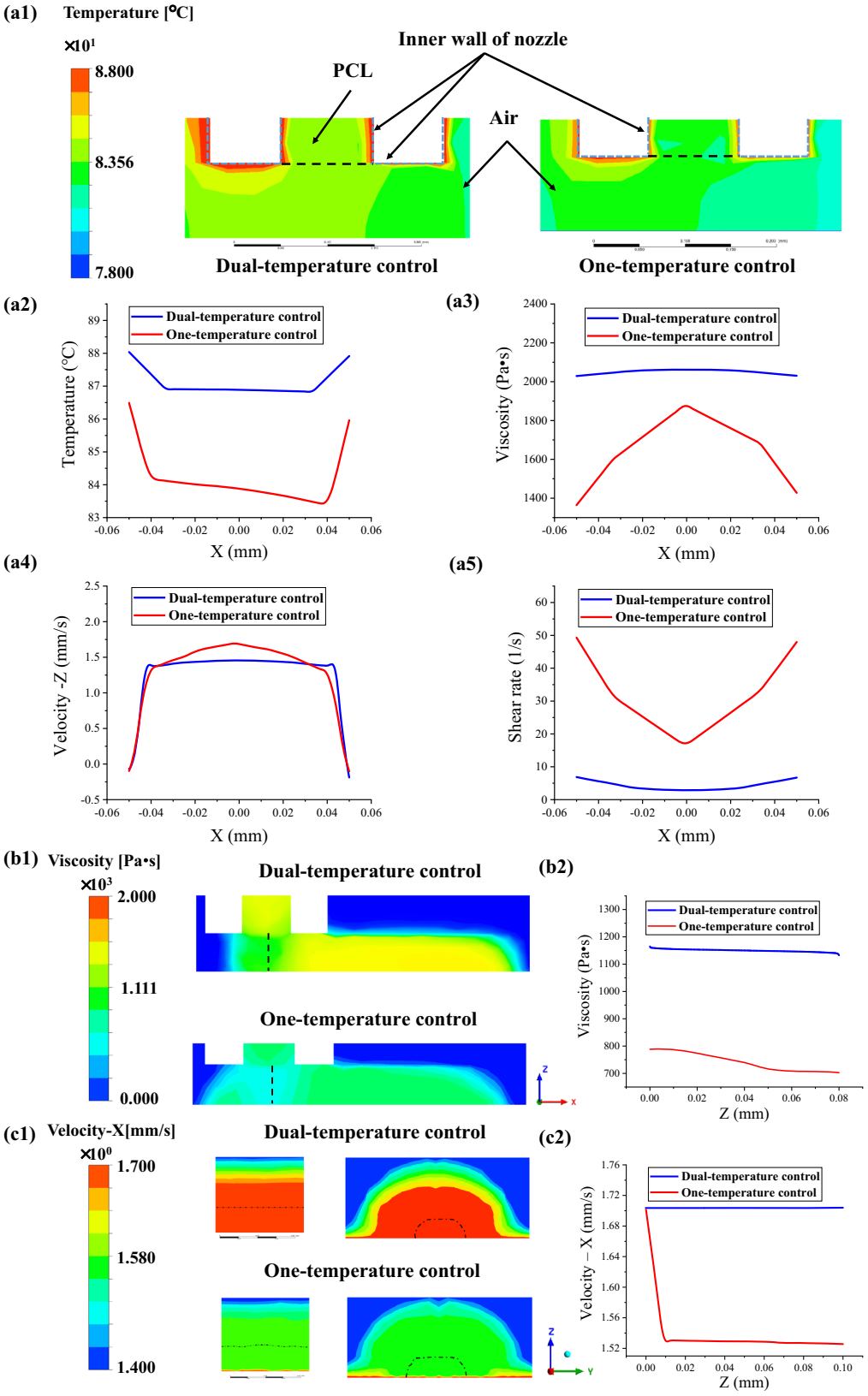


**Fig. 4** Mechanistic analysis of filament printing: **a1** contour of temperature (the black dotted line represents the diagram of the exported data line), **a2** temperature, **a3** viscosity, **a4** velocity at $z$-direction, and **a5** shear rate at the nozzle outlet; **b1** contour of viscosity at $t$=0.5 s and **b2** viscosity distribution at $z$-direction; **c1** contour of velocity at $x$-direction and **c2** velocity distribution of $x$-direction of $z$-direction melted poly(ε-caprolactone) (PCL) when printing speed $v$=1.7 mm/s

less uniform with one-temperature control (Fig. 4b2), resulting in a velocity gradient in the $x$-direction of the $z$-direction deposited PCL filament (Fig. 4c2). The velocity gradient leads to the shear rate between layers, which leads to unstable filament formation (Fig. 3a).

## PCL deposition at corners

The deposition of ink at the corners significantly affects the geometric quality of parts fabricated by extrusion printing. To quantify the corner filling performance, we propose a dimensionless number to evaluate the deviation between the design and the actual path as (Fig. 5b1),

$$A_{\mathrm{d}} = \frac{A_{\mathrm{deviation}}}{A_{\mathrm{design}}}, \tag{6}$$

where $A_{\mathrm{deviation}}$=$A_{\mathrm{overfill}}$+$A_{\mathrm{underfill}}$, and $A_{\mathrm{design}}$ is the designed area. The deviation area ($A_{\mathrm{deviation}}$) consists of two parts: one part is the amount of overfill ($A_{\mathrm{overfill}}$), and the other is that of underfill ($A_{\mathrm{underfill}}$). As $A_{\mathrm{d}}$ decreases to 0, the deposition of PCL at the corner is closer to the designed path, resulting in an excellent geometric quality of the corner. Figure 5a shows that the filling quality of the corner worsens with increasing printing speed. At the same printing speed, the temperature control of the corner filling performance is better with the dual-temperature control FDM than with the one-temperature control FDM (Fig. 5b2). In addition, the numerical results agree well with the experimental results (Fig. 5a).

To understand the mechanism of the smaller deviation of dual-temperature control FDM, we use a numerical model with a printing speed of 1.6 mm/s for analysis. Notably, regardless of moving in the $x$-direction (Fig. 5c1) or the $y$-direction (Fig. 5c2), the velocity gradient is smaller in the dual-temperature control FDM. Based on the viscosity distribution at the outlet, the viscosity of the melted PCL in dual-temperature control FDM is larger than that of the one-temperature control FDM; when the viscosity of the melted PCL is larger, the speed of filament deposition is closer to the printing speed. When printing from the $x$- to $y$-direction, the velocity gradient in the latter bends the filament, and the bending degree increases with the velocity gradient. Therefore, the design and the actual path show a slight difference in the dual-temperature control FDM.

## Filament fusion test

Instead of maintaining the 3D constructs, the two adjacent filaments are fused, which significantly influences the printing resolution. The resolution of the printed filaments in the $x$–$y$ plane was assessed by measuring their width ($W$), gap ($G$), and fusion length ($F$) (Fig. 6c). Notably, filaments fuse when they have a small gap distance (Fig. 6a). Thus, $F/W$ is defined as the degree of filament fusion, and $F/W$=1 indicates that the filaments at the corner have the same width along both the $x$ and $y$ directions and that no fusion occurs. When $F/W$ decreases, the width of the filaments in the two vertical directions tends to be close, and the deposited filaments have a higher shape fidelity. Figure 6b shows that the values of $F/W$ in the dual-temperature control FDM are smaller than those in the one-temperature control FDM, which means that dual-temperature control can improve the printability of PCL in FDM.

The filament fusion test is performed by printing the 90° corner, and its quality is assessed by using the corner length ($L_{\mathrm{c}}$) (Fig. 6c1), which refers to the deviation between the actual and designed paths. Notably, when $G$<$W$, the filaments completely fused (Fig. 6c2); when $W$<$G$<$L_{\mathrm{c}}$, the filaments only fused at the corner (Fig. 6c3); when $G$>$L_{\mathrm{c}}$, the filament did not fuse, and $F/W$≈1 (Fig. 6c4). When the printing speed is 1.0 mm/s, $W_1$ is 138 μm and $L_{\mathrm{c1}}$ is 630 μm with the one-temperature control FDM, while $W_2$ is 132 μm and $L_{\mathrm{c2}}$ is 310 μm with the dual-temperature control FDM (Fig. 6d1). Changes in $G$ lead to four results (Fig. 6d2): (1) when $L_{\mathrm{c1}}$<$G$ < $L_{\mathrm{c2}}$, the filament does not fuse; (2) when $W_1$ < $G$ < $L_{\mathrm{c1}}$, and $G$ > $L_{\mathrm{c2}}$, filament fusion occurs with one-temperature control but not with dual-temperature control; (3) when $W_1$<$G$<$L_{\mathrm{c1}}$, and $W_2$<$G$<$L_{\mathrm{c2}}$, filament fusion occurs in both temperature modes; and (4) when $G$ < $W_1$, and $G$ < $W_2$, complete filament fusion is found in two modes.

## Filament collapse test

To quantify the effects of different printing speeds and spanning distances on filament collapse, a filament collapse test was performed (Fig. 7a). Here, this study introduces the collapse distance, which is the distance between the lowest point of collapse and the substrate. The collapse distance gradually increases with the spanning distance at the same printing speed (Fig. 7c1) but gradually decreases with increasing printing speed at the same spanning distance (Fig. 7c2). In addition, the collapse distance in the one-temperature control FDM is always larger than that in the dual-temperature control FDM with the same printing parameters (Fig. 7c). Therefore, the dual-temperature control FDM of PCL provided a better shape fidelity of PCL scaffolds than the one-temperature control FDM.

The deformation of the suspended filaments is caused by the weight of the material. Given that the high viscosity of melted PCL leads to a smaller deformation caused by gravity and that the viscosity of melted PCL in one-temperature control FDM is lower than that in dual-temperature control FDM (Fig. 7d), the collapse distance is larger in one-temperature control FDM.

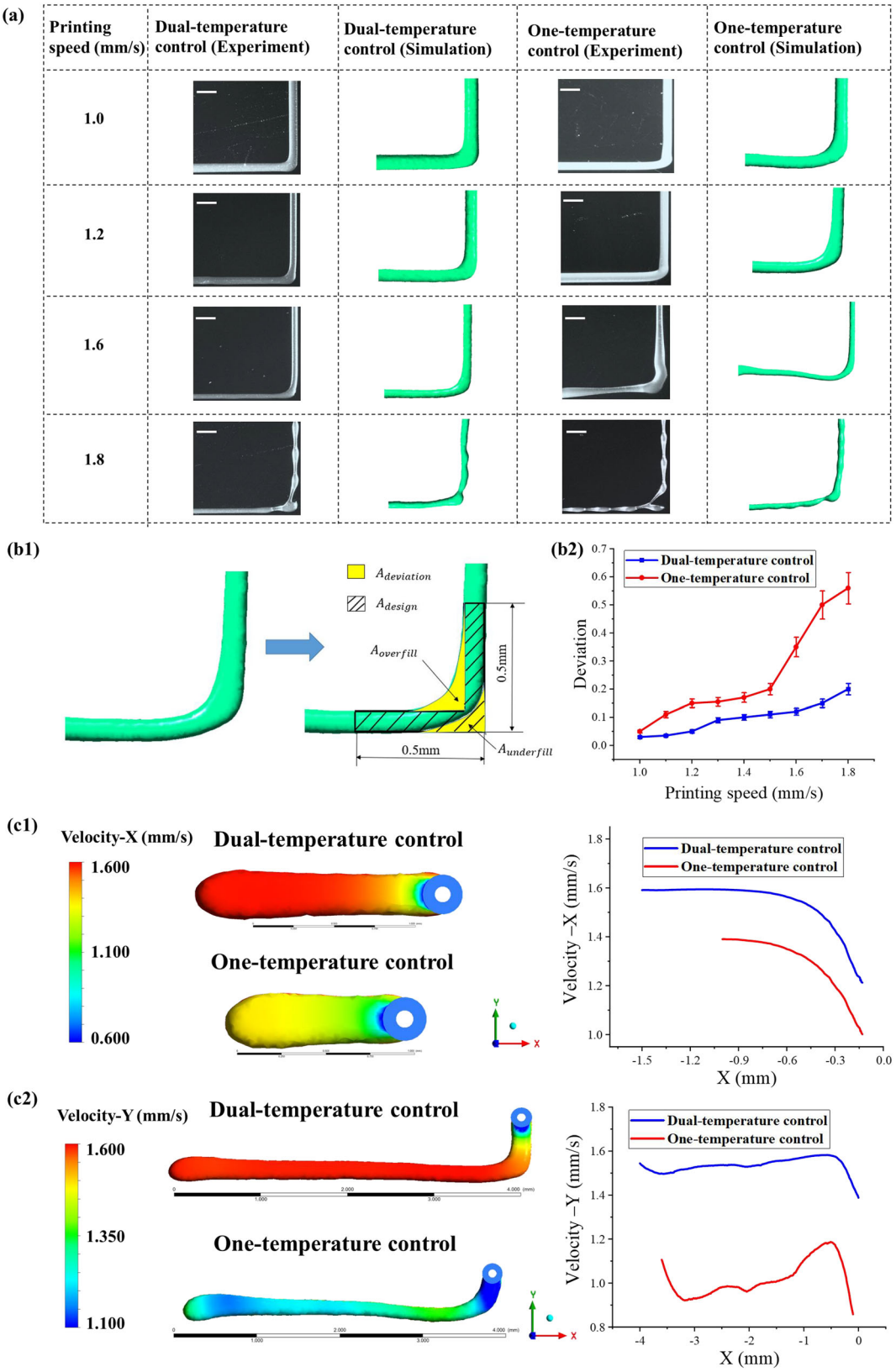


**Fig. 5** Filament deposition at corners: **a** experimental and simulated results; **b1** schematic diagram of the calculation of the deviation amount, scale bar=200 μm, and **b2** plot of deviation as a function of printing speed. When printing speed $v$=1.6 mm/s: **c1** velocity in the $x$-direction when $t$=1 s and **c2** velocity in the $y$-direction when $t$=2.8 s

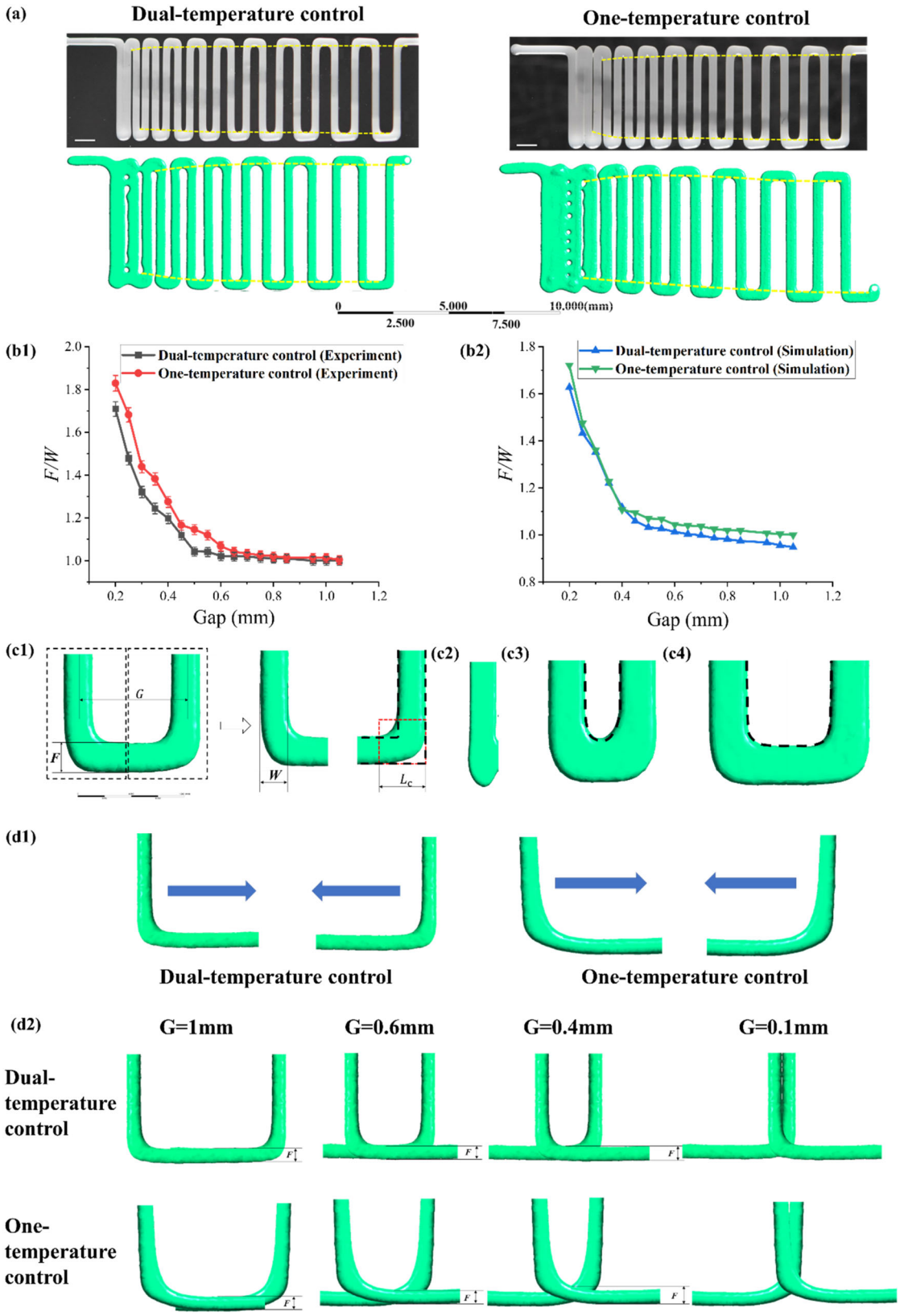


**Fig. 6** Exploration of the filament fusion test: **a** experimental and simulated results when printing speed $v$=1.0 mm/s, scale bar=300 μm; $F/W$ as a function of gap with dual- and one-temperature control: **b1** experimental results and **b2** simulated results; **c1** exploded view, **c2** complete fusion between filaments, **c3** fusion between filaments at the corners, **c4** no fusion between filaments; **d1** schematic diagram of filament fusion test explained by deposition at corners and **d2** filament fusion test with gap changes

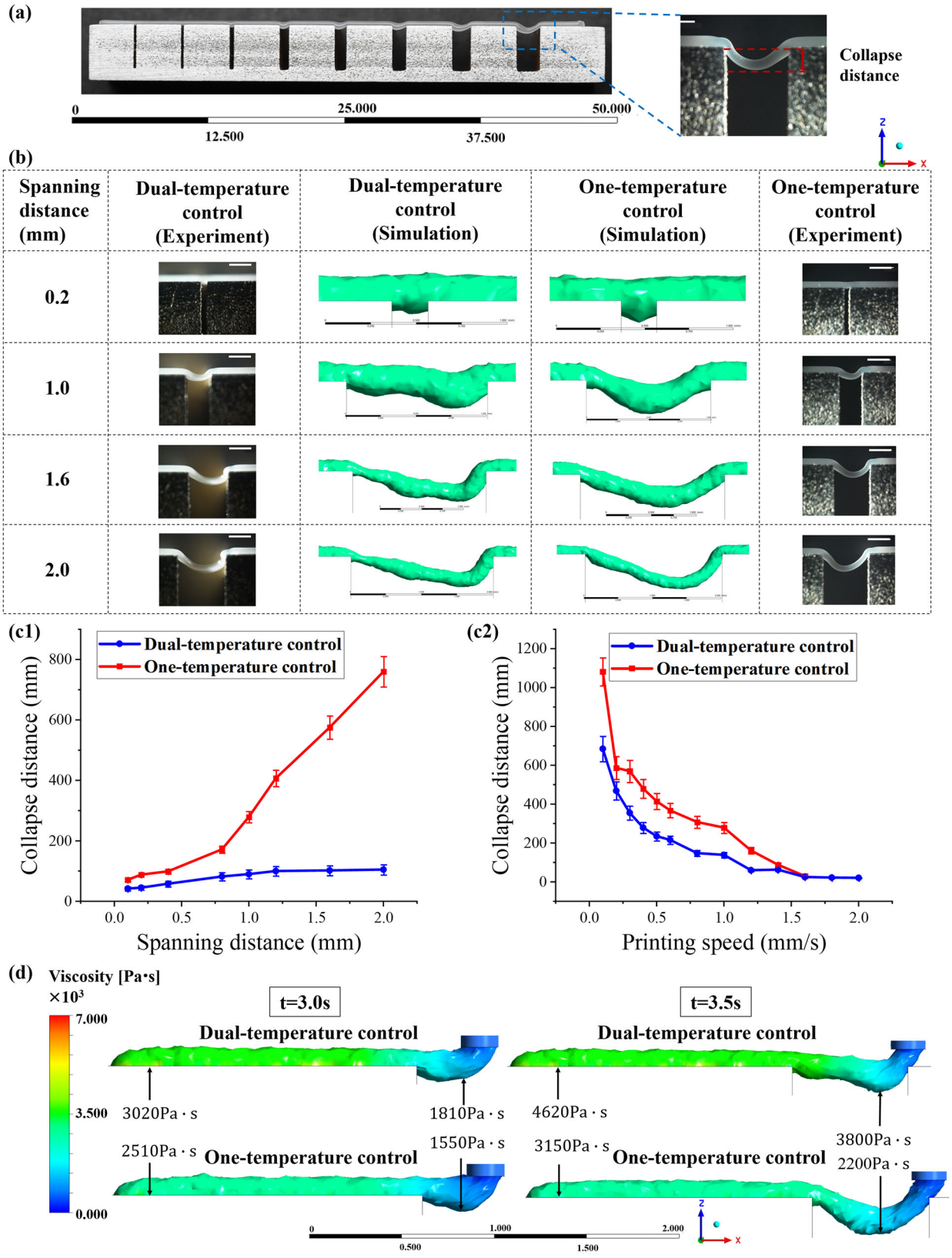


**Fig. 7** Exploring the mechanism of filament collapse: **a** substrate model, scale bar=600 μm; **b** results based on dual- and one-temperature control, scale bar=1 mm; **c1** when printing speed=1.0 mm/s, the collapse distance changes with the spanning distance; **c2** when spanning distance=1.0 mm, the collapse distance changes with the speed of the substrate (the blue line represents the result with dual-temperature control, and the red line represents the result with one-temperature control); **d** viscosity contours at different times

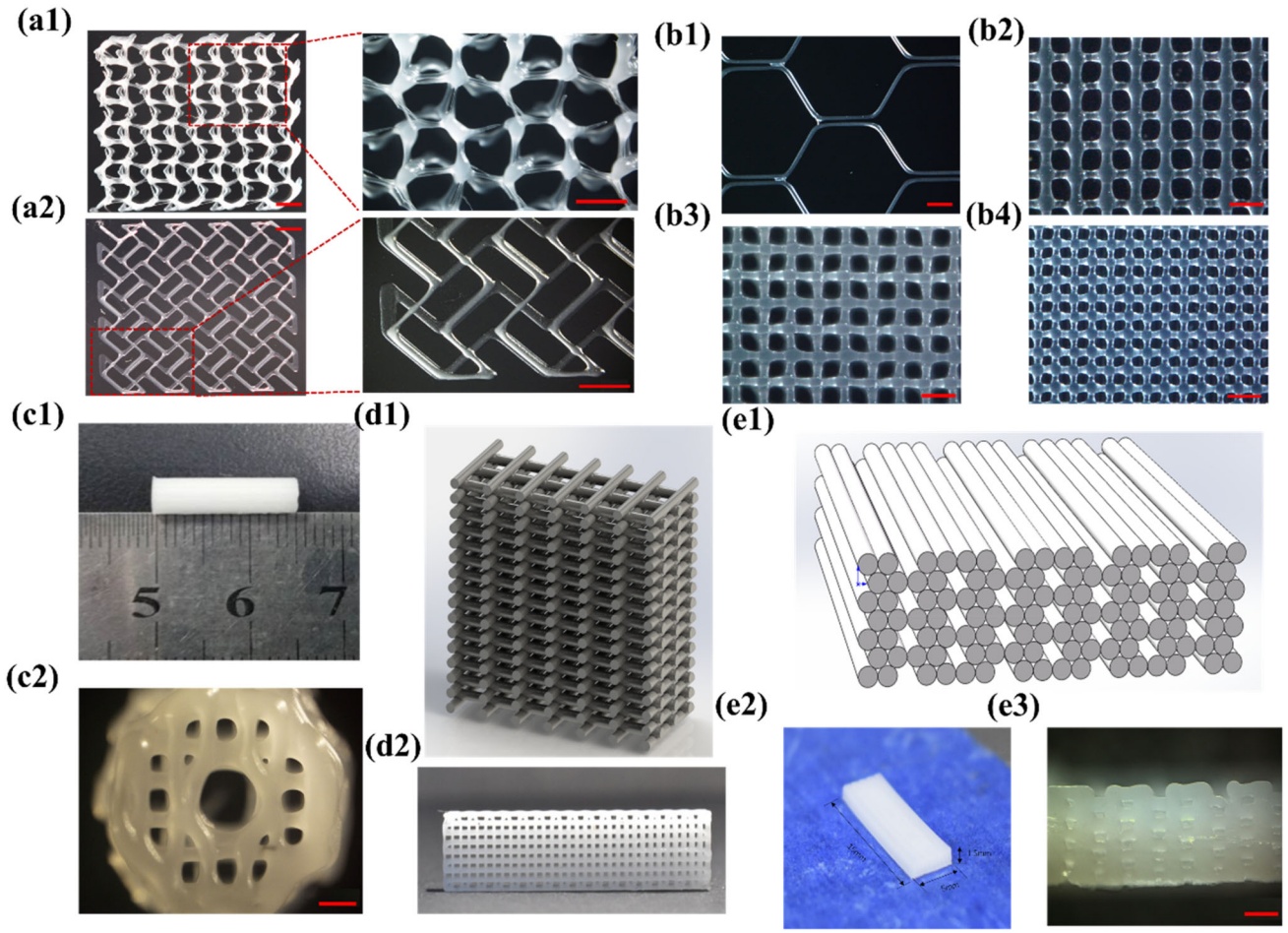


**Fig. 8** Structures printed with dual-temperature control: **a1** hexagonal architecture, scale bar=600 μm and **a2** zigzag architecture, scale bar=600 μm; **b1** hexagonal scaffold with one layer when the printing speed is 1.0 mm/s, scale bar=200 μm. Rectangular scaffold when printing speed is **b2** 0.2 mm/s, **b3** 0.3 mm/s, and **b4** 0.5 mm/s, scale bar=200 μm; **c1** length of the tube scaffold and **c2** micrograph of the cross section of the tube scaffold, scale bar=500 μm; **d1** schematic diagram of the square scaffold and **d2** image of the PCL square scaffold; **e1** schematic of the PCL tendon scaffold, **e2** image of the PCL tendon scaffold, and **e3** micrograph of the PCL tendon scaffold, scale bar=600 μm. PCL: poly(ε-caprolactone)

## Demonstration of dual-temperature control FDM

All structures in Fig. 8 are printed by the dual-temperature control FDM. Figure 8a1 shows the structure of the hexagonal network, and Fig. 8a2 shows the architecture formed by zigzag mesh (inner diameter of the nozzle $D$=100 μm). Figure 8b also shows the PCL scaffolds printed by the dual-temperature control FDM using the nozzle with an inner diameter of 60 μm. The hexagonal scaffold was printed when the printing speed was 1.0 mm/s (Fig. 8b1). Figure 8c shows a tube scaffold with a diameter of 3.8 mm and a height of 15 mm (inner diameter of the nozzle $D$=200 μm). Figure 8d is a PCL square scaffold (10 mm×5 mm×5 mm, $D$=10 μm). Figure 8e shows the schematic diagram and image of the tendon scaffold (15 mm×5 mm×1.5 mm, $D$=200 μm). The dual-temperature control FDM shows precise manufacturing and spatially arranged constructs and is a highly efficient tool for generating bioengineered structures. Therefore, dual-temperature control FDM significantly extends 3D printing in future scaffold applications.

## Conclusions

Scaffolds with high porosity and specific surface area used in tissue engineering significantly influence the physiological activities of cell survival, migration, proliferation, and differentiation. In this study, a dual-temperature control method is proposed to improve the resolution of FDM printing. The deposited PCL filament with a width of 50 μm is achieved by using a nozzle with an inner diameter of 100 μm. More

importantly, a numerical model is developed by implementing the constitutive model, in which the viscosity is a function of temperature and shear rate, and both numerical and experimental investigations are carried out to study the influence of two different temperature control modes on viscosity. By comparing the results of 1D, 2D, and 3D PCL printing, the dual-temperature control mode provides a higher viscosity and lower velocity gradient of deposited PCL during FDM printing, leading to better printing with satisfactory accuracy. Therefore, the dual-temperature control FDM presents a promising application of PCL FDM in tissue engineering.

**Acknowledgements** The authors gratefully acknowledge the support provided by the National Natural Science Foundation of China (Nos. 52250006 and 52075482) and the Starry Night Science Fund of Zhejiang University Shanghai Institute for Advanced Study (No. SN-ZJU-SIAS-004).

**Author contributions** XDH and BZ performed 3D printing experiments; XDH, JY, and QLH developed numerical model; YH and JY wrote the original draft and revised the manuscript.

## Declarations

**Conflict of interest** The authors declare that they have no conflict of interest.

**Ethical approval** This study does not contain any studies with human or animal subjects performed by any of the authors.

## References

1. Santoro M, Shah SR, Walker JL et al (2016) Poly(lactic acid) nanofibrous scaffolds for tissue engineering. Adv Drug Deliv Rev 107:206–212. https://doi.org/10.1016/j.addr.2016.04.019
2. Siddiqui N, Asawa S, Birru B et al (2018) PCL-based composite scaffold matrices for tissue engineering applications. Mol Biotechnol 60(7):506–532. https://doi.org/10.1007/s12033-018-0084-5
3. Zhao W, Li J, Jin K et al (2016) Fabrication of functional PLGA-based electrospun scaffolds and their applications in biomedical engineering. Mater Sci Eng C 59:1181–1194. https://doi.org/10.1016/j.msec.2015.11.026
4. Roseti L, Parisi V, Petretta M et al (2017) Scaffolds for bone tissue engineering: state of the art and new perspectives. Mater Sci Eng C Mater Biol Appl 78:1246–1262. https://doi.org/10.1016/j.msec.2017.05.017
5. Zhang Y, Liu X, Zeng L et al (2019) Polymer fiber scaffolds for bone and cartilage tissue engineering. Adv Funct Mater 29(36):1903279. https://doi.org/10.1002/adfm.201903279
6. Hutmacher DW (2001) Scaffold design and fabrication technologies for engineering tissues-state of the art and future perspectives. J Biomater Sci Polym Ed 12(1):107–124. https://doi.org/10.1163/156856201744489
7. Jakus AE, Geisendorfer NR, Lewis PL et al (2018) 3D-printing porosity: a new approach to creating elevated porosity materials and structures. Acta Biomater 72:94–109. https://doi.org/10.1016/j.actbio.2018.03.039
8. Safaei F, Khalili S, Nouri Khorasani S et al (2018) Porogen effect of solvents on pore size distribution of solvent-casted polycaprolactone thin films. J Polym Sci Eng 1(4):1076. https://doi.org/10.24294/jpse.v1i4.1076
9. Mooney DJ, Baldwin DF, Suh NP et al (1996) Novel approach to fabricate porous sponges of poly(D, L-lactic-co-glycolic acid) without the use of organic solvents. Biomaterials 17(14):1417–1422. https://doi.org/10.1016/0142-9612(96)87284-X
10. Schugens C, Maquet V, Grandfils C et al (1996) Polylactide macroporous biodegradable implants for cell transplantation. II. Preparation of polylactide foams by liquid-liquid phase separation. J Biomed Mater Res 30(4):449–461. https://doi.org/10.1002/(SICI)1097-4636(199604)30:4<449::AID-JBM3>3.0.CO;2-P
11. Park JY, Choi YJ, Shim JH et al (2017) Development of a 3D cell printed structure as an alternative to autologs cartilage for auricular reconstruction. J Biomed Mater Res Part B Appl Biomater 105(5):1016–1028. https://doi.org/10.1002/jbm.b.33639
12. Meng Z, He J, Li J et al (2020) Melt-based, solvent-free additive manufacturing of biodegradable polymeric scaffolds with designer microstructures for tailored mechanical/biological properties and clinical applications. Virtual Phys Prototyp 15(4):417–444. https://doi.org/10.1080/17452759.2020.1808937
13. Olubamiji AD, Izadifar Z, Si JL et al (2016) Modulating mechanical behaviour of 3D-printed cartilage-mimetic PCL scaffolds: influence of molecular weight and pore geometry. Biofabrication 8(2):25020. https://doi.org/10.1088/1758-5090/8/2/025020
14. Meng Z, He J, Li D (2021) Additive manufacturing and large deformation responses of highly-porous polycaprolactone scaffolds with helical architectures for breast tissue engineering. Virtual Phys Prototyp 16(3):291–305. https://doi.org/10.1080/17452759.2021.1930069
15. Hrynevich A, Elçi BŞ, Haigh JN et al (2018) Dimension-based design of melt electrowritten scaffolds. Small 14(22):e1800232. https://doi.org/10.1002/smll.201800232
16. Wüst S, Müller R, Hofmann S (2011) Controlled positioning of cells in biomaterials—approaches towards 3D tissue printing. J Funct Biomater 2(3):119–154. https://doi.org/10.3390/jfb2030119
17. Saygili E, Dogan-Gurbuz AA, Yesil-Celiktas O et al (2020) 3D bioprinting: a powerful tool to leverage tissue engineering and microbial systems. Bioprinting 18:e00071. https://doi.org/10.1016/j.bprint.2019.e00071
18. Melchels FPW, Domingos MAN, Klein TJ et al (2012) Additive manufacturing of tissues and organs. Progr Polym Sci 37(8):1079–1104. https://doi.org/10.1016/j.progpolymsci.2011.11.007
19. Guillemot F, Mironov V, Nakamura M (2010) Bioprinting is coming of age: report from the International Conference on Bioprinting and Biofabrication in Bordeaux (3B'09). Biofabrication 2(1):010201. https://doi.org/10.1088/1758-5082/2/1/010201
20. Ligon SC, Liska R, Stampfl J et al (2017) Polymers for 3D printing and customized additive manufacturing. Chem Rev 117(15):10212–10290. https://doi.org/10.1021/acs.chemrev.7b00074
21. Wickramasinghe S, Do T, Tran P (2020) FDM-based 3D printing of polymer and associated composite: a review on mechanical properties, defects and treatments. Polymers 12(7):1529. https://doi.org/10.3390/polym12071529
22. Reiner T, Carr N, Měch R et al (2014) Dual-color mixing for fused deposition modeling printers. Comput Graph Forum 33(2):479–486. https://doi.org/10.1111/cgf.12319
23. Mohamed OA, Masood SH, Bhowmik JL (2015) Optimization of fused deposition modeling process parameters: a review of current research and future prospects. Adv Manuf 3(1):42–53. https://doi.org/10.1007/s40436-014-0097-7

24. Serdeczny MP, Comminal R, Pedersen DB et al (2018) Experimental validation of a numerical model for the strand shape in material extrusion additive manufacturing. Addit Manuf 24:145–153. https://doi.org/10.1016/j.addma.2018.09.022
25. Yin J, Lu C, Fu J et al (2018) Interfacial bonding during multi-material fused deposition modeling (FDM) process due to inter-molecular diffusion. Mater Des 150:104–112. https://doi.org/10.1016/j.matdes.2018.04.029
26. Awasthi P, Banerjee SS (2021) Fused deposition modeling of thermoplastic elastomeric materials: challenges and opportunities. Addit Manuf 46:102177. https://doi.org/10.1016/j.addma.2021.102177
27. Wang X, Jiang M, Zhou Z et al (2017) 3D printing of polymer matrix composites: a review and prospective. Compos Part B Eng 110:442–458. https://doi.org/10.1016/j.compositesb.2016.11.034
28. Ang KC, Leong KF, Chua CK et al (2006) Investigation of the mechanical properties and porosity relationships in fused deposition modelling-fabricated porous structures. Rapid Prototyp J 12(2):100–105. https://doi.org/10.1108/13552540610652447
29. Yang S, Leong KF, Du Z et al (2002) The design of scaffolds for use in tissue engineering. Part II. Rapid prototyping techniques. Tissue Eng 8(1):1–11. https://doi.org/10.1089/107632702753503009
30. Leong KF, Cheah CM, Chua CK (2003) Solid freeform fabrication of three-dimensional scaffolds for engineering replacement tissues and organs. Biomaterials 24(13):2363–2378. https://doi.org/10.1016/s0142-9612(03)00030-9
31. Phan DD, Horner JS, Swain ZR et al (2020) Computational fluid dynamics simulation of the melting process in the fused filament fabrication additive manufacturing technique. Addit Manuf 33:101161. https://doi.org/10.1016/j.addma.2020.101161
32. Gao T, Gillispie GJ, Copus JS et al (2018) Optimization of gelatin-alginate composite bioink printability using rheological parameters: a systematic approach. Biofabrication 10(3):34106. https://doi.org/10.1088/1758-5090/aacdc7
33. Comminal R, Serdeczny MP, Pedersen DB et al (2018) Numerical modeling of the strand deposition flow in extrusion-based additive manufacturing. Addit Manuf 20:68–76. https://doi.org/10.1016/j.addma.2017.12.013
34. Zein I, Hutmacher DW, Tan KC et al (2002) Fused deposition modeling of novel scaffold architectures for tissue engineering applications. Biomaterials 23(4):1169–1185. https://doi.org/10.1016/s0142-9612(01)00232-0
35. Zhang ZZ, Jiang D, Ding JX et al (2016) Role of scaffold mean pore size in meniscus regeneration. Acta Biomater 43:314–326. https://doi.org/10.1016/j.actbio.2016.07.050
36. Wang Q, Ma Z, Wang Y et al (2021) Fabrication and characterization of 3D printed biocomposite scaffolds based on PCL and zirconia nanoparticles. Bio-Des Manuf 4(1):60–71. https://doi.org/10.1007/s42242-020-00095-3
37. Manjunath KS, Sridhar K, Gopinath V et al (2020) Facile manufacturing of fused-deposition modeled composite scaffolds for tissue engineering—an embedding model with plasticity for incorporation of additives. Biomed Mater 16(1):15028. https://doi.org/10.1088/1748-605x/abc1b0
38. Hollister SJ (2005) Porous scaffold design for tissue engineering. Nat Mater 4(7):518–524. https://doi.org/10.1038/nmat1421
39. Karageorgiou V, Kaplan D (2005) Porosity of 3D biomaterial scaffolds and osteogenesis. Biomaterials 26(27):5474–5491. https://doi.org/10.1016/j.biomaterials.2005.02.002
40. Wang C, Huang W, Zhou Y et al (2020) 3D printing of bone tissue engineering scaffolds. Bioact Mater 5(1):82–91. https://doi.org/10.1016/j.bioactmat.2020.01.004
41. Zaszczyńska A, Moczulska-Heljak M, Gradys A et al (2021) Advances in 3D printing for tissue engineering. Materials 14(12):3149. https://doi.org/10.3390/ma14123149
42. Shanmugam V, Pavan MV, Babu K et al (2021) Fused deposition modeling based polymeric materials and their performance: a review. Polym Compos 42(11):5656–5677. https://doi.org/10.1002/pc.26275
43. Cano-Vicent A, Tambuwala MM, Hassan SS et al (2021) Fused deposition modelling: current status, methodology, applications and future prospects. Addit Manuf 47:102378. https://doi.org/10.1016/j.addma.2021.102378
44. Kumar N, Jain PK, Tandon P et al (2018) Investigation on the effects of process parameters in CNC assisted pellet based fused layer modeling process. J Manuf Process 35:428–436. https://doi.org/10.1016/j.jmapro.2018.08.029
45. Hıra O, Yücedağ S, Samankan S et al (2022) Numerical and experimental analysis of optimal nozzle dimensions for FDM printers. Progr Addit Manuf 7:823–838. https://doi.org/10.1007/s40964-021-00241-y
46. Ketabdari MJ, Saghi H (2013) Development of volume of fluid methods to model free surface flow using new advection algorithm. J Brazilian Soc Mech Sci Eng 35(4):479–491. https://doi.org/10.1007/s40430-013-0045-7
47. Hirt CW, Nichols BD (1981) Volume of fluid (VOF) method for the dynamics of free boundaries. J Comput Phys 39(1):201–225. https://doi.org/10.1016/0021-9991(81)90145-5
48. Saghi H, Ketabdari MJ, Zamirian M (2013) A novel algorithm based on parameterization method for calculation of curvature of the free surface flows. Appl Math Model 37(1):570–585. https://doi.org/10.1016/j.apm.2012.02.043
49. Rohlfs W, Dietze GF, Haustein HD et al (2012) Two-phase electrohydrodynamic simulations using a volume-of-fluid approach: a comment. J Comput Phys 231(12):4454–4463. https://doi.org/10.1016/j.jcp.2012.02.003
50. Saghi H, Ketabdari MJ (2014) A modification to SLIC and PLIC volume of fluid models using new advection method. Arab J Sci Eng 39(2):669–684. https://doi.org/10.1007/s13369-013-0688-9
51. Cross MM (1979) Relation between viscoelasticity and shear-thinning behaviour in liquids. Rheol Acta 18(5):609–614. https://doi.org/10.1007/BF01520357
52. Chiang HH, Hieber CA, Wang KK (1991) A unified simulation of the filling and postfilling stages in injection molding. Part I: Formulation. Polym Eng Sci 31:116–124. https://doi.org/10.1002/pen.760310210
53. Song K, Zhang D, Yin J et al (2021) Computational study of extrusion bioprinting with jammed gelatin microgel-based composite ink. Addit Manuf 41:101963. https://doi.org/10.1016/j.addma.2021.101963